

**Self-similar decay of the drag wake of a dimpled sphere**D. Curtis Saunders,<sup>1,\*</sup> Gary Frederick,<sup>1</sup> Theodore D. Drivas<sup>2</sup>,<sup>1</sup> and Scott Wunsch<sup>1</sup><sup>1</sup>*The Johns Hopkins University Applied Physics Laboratory, Laurel, Maryland 20723, USA*<sup>2</sup>*Department of Mathematics, Princeton University, Princeton, New Jersey 08544, USA*(Received 27 April 2020; accepted 30 November 2020;  
published 21 December 2020)

The drag wake of a dimpled sphere is studied experimentally using stereo particle image velocimetry at  $Re = 5 \times 10^4$  to a downstream distance of  $\sim 200$  diameters. The wake growth and velocity decay are analyzed and compared with self-similar decay laws. The measured exponents for the mean axial velocity field differ from the classical mean-field self-similar solution. This is consistent with other recent experimental observations of the near wake of axisymmetric bodies but is the first to show a full decade of scaling with nonclassical exponents, indicating the scaling is not merely a near-wake effect. The data also indicate that deviations from the classical solution may be due to the failure of the assumption that velocity fluctuations are in balance with production from the mean axial flow. Relaxing this assumption yields a family of self-similar decay solutions, one of which is consistent with the measured wake decay. The observed solution preserves the velocity fluctuation Reynolds number with downstream distance. The experimental data also show that individual wake realizations bear little resemblance to the mean flow, suggesting that mean flow solutions may have limited practical value.

DOI: [10.1103/PhysRevFluids.5.124607](https://doi.org/10.1103/PhysRevFluids.5.124607)**I. INTRODUCTION**

The spreading and decay of the drag wake of an object is of interest to a wide variety of applications in geophysics and engineering, such as the wakes of mountains, seamounts, windmills, and buildings. For axisymmetric bodies, the classical self-similar scaling law [1,2] has long been used to describe the wakes of spheres [3] and slender bodies [4] at laboratory scales. However, some recent wake experiments have cast doubt on the classical decay law [5,6] with results indicating more rapid wake spreading and decay than proposed in Refs. [1,2]. Some of these experiments indicate that rough shapes (fractals) deviate from classical scaling whereas more smooth shapes do not [6]. High-resolution numerical simulations have also reproduced the more rapid nonclassical wake spreading [7,8]. Various explanations for this novel wake behavior have been offered. One possibility, proposed by Refs. [6,9,10], is a modification of the standard scaling of the dissipation rate  $\varepsilon \sim K^{3/2}/L$ , where  $K$  is the turbulent kinetic energy and  $L$  is the length scale of turbulent eddies [2]. Another is nonequilibrium fluctuations around the Kolmogorov turbulence spectrum [11]. Nonclassical scaling may also be attributed to low-Reynolds (Re) number (viscous) effects as in Refs. [12,13]. It has also been suggested that nonclassical and classical scalings are a function of local Reynolds number [13] or downstream distance [8].

Nonclassical decay of the drag wake of a sphere was first reported experimentally by Ref. [5] and in numerical simulation by Ref. [7]. These results contradict the earlier experimental sphere wake results of Ref. [3]. The sphere data of Ref. [5] were collected for a Reynolds number ( $U_m D/\nu$ ,

\*Corresponding author: [Curtis.Saunders@jhuapl.edu](mailto:Curtis.Saunders@jhuapl.edu)

where  $D$  is the sphere diameter and  $U_m$  is the tow velocity) of  $1.2 \times 10^4$ . They demonstrated that the velocity wake defect decay exponent was approximately  $-1$  to a distance of  $x/D \sim 30$  but could not determine if this exponent persisted farther downstream or was merely a transitory near-wake effect. This exponent was in approximate agreement with the subsequent fractal wake data of Ref. [6], which modestly extended the experimentally observed nonclassical scaling range to  $x/D \sim 50$  as well as the simulations of Refs, [7,8]. Here, stereo particle image velocimetry (SPIV) measurements of a dimpled (rough) sphere wake are performed at a Reynolds number of  $5 \times 10^4$  with velocity decay measurements to  $x/D \sim 200$ . This extends the limit of experimental observations four times farther than previous axisymmetric wake studies, allowing for a full decade of scaling to determine if nonclassical decay is a near-wake effect. As described below, these results confirm that more rapid wake decay first reported by Ref. [5] extends to, at least,  $x/D \sim 200$ . Additional measurements show the growth of the wake width and the decay of velocity fluctuations. These additional results, which were not obtained by previous experimental studies, prove helpful in characterizing the nonclassical wake decay.

A fairly conventional explanation for the experimentally observed scaling is proposed here, which (unlike Refs. [6,9,10]) is consistent with the standard dissipation assumption. In this model, the nonclassical decay occurs because the initial wake velocity fluctuations dominate over production by the mean shear, decoupling these terms in the standard Reynolds-averaged self-similar wake theory. The wake fluctuations then grow more rapidly than the classical result. Whether this scaling persists indefinitely, or transitions to the classical law as suggested by Ref. [8], remains an open question, but the data do not indicate that any such crossover occurs prior to  $x/D \sim 200$ .

## II. SELF-SIMILAR WAKE DECAY THEORY

Here, the standard self-similar theory for axisymmetric drag wake decay is outlined to illustrate the implications of different closure assumptions. Following Ref. [12], as in Refs. [6,10], the axisymmetric drag wake is described by ensemble-averaged equations for the momentum and energy:

$$U_m \frac{\partial}{\partial x} (U_m - U) = -\frac{1}{r} \frac{\partial}{\partial r} (r \overline{uv}), \quad (1)$$

$$U_m \frac{\partial}{\partial x} \left( \frac{1}{2} \overline{q^2} \right) = -\overline{uv} \frac{\partial U}{\partial r} - \frac{1}{r} \frac{\partial}{\partial r} \left[ r \left( \frac{1}{2} v \overline{q^2} + \frac{\overline{pv}}{\rho} \right) \right] - \varepsilon, \quad (2)$$

where  $q^2 = u^2 + v^2 + w^2$  is the velocity fluctuation squared (i.e., the deviation from the ensemble mean),  $U$  is the ensemble-mean streamwise velocity,  $U_m$  is the tow velocity,  $x$  is the downstream distance, and  $\varepsilon$  is the energy dissipation rate. The  $q^2$  term is sometimes referred to as ‘‘turbulent kinetic energy,’’ but in this nonstationary (decaying) flow it is best interpreted as the fluctuation from the ensemble mean since the concept of mean and fluctuation are only defined in the ensemble. As in Refs, [6,12], a self-similar solution is assumed in the far-wake region,

$$U_m - U = U_o(x)f(\eta), \quad (3)$$

$$\frac{1}{2} \overline{q^2} = K(x)h(\eta), \quad (4)$$

$$\overline{uv} = R(x)g(\eta), \quad (5)$$

$$\frac{1}{2} u \overline{q^2} + \frac{\overline{pv}}{\rho} = T(x)\tau(\eta), \quad (6)$$

$$\varepsilon = \epsilon(x)\chi(\eta), \quad (7)$$

where  $U_o(x)$ ,  $K(x)$ ,  $R(x)$ ,  $T(x)$ , and  $\epsilon(x)$  are the self-similar scales for mean axial velocity, velocity fluctuation, Reynolds stress, kinetic-energy production, and dissipation rate, respectively. The dimensionless radial similarity coordinate is  $\eta \equiv r/L$ ,  $L(x)$  is the ‘‘size’’ of the wake, and  $f(\eta)$

TABLE I. Exponent comparison: theory.

Quantity	Classical [1,2]	Viscous [12,13]	Anomalous [6]	Proposed
Wake size $L$	1/3	1/2	1/2	$\alpha$
Velocity defect $U_o$	-2/3	-1	-1	$-2\alpha$
Turbulent kinetic-energy $K$	-4/3	-2	-2	$2(\alpha - 1)$
Reynolds stress $R$	-4/3	-3/2	-3/2	$-(\alpha + 1)$
Dissipation rate $\epsilon$	-7/3		-3	$2\alpha - 3$

is the similarity shape function for mean axial velocity. The other functions of  $\eta$  are shape functions for their respective quantities. Substituting these into Eq. (2) and comparing the  $x$  dependence of each term yields the following solvability conditions:

$$\frac{\partial L}{\partial x} \sim \frac{\epsilon L}{KU_m} \sim \frac{T}{KU_m} \sim \frac{RU_o}{KU_m}. \quad (8)$$

These conditions were also found in Refs. [2,6,12], who assumed all of these terms scaled together. Likewise, Eq. (1) yields the momentum conservation constraint for a drag wake,  $U_o L^2 = (\text{const})$  as well as the additional solvability condition  $R \sim U_o U_m \partial_x L$ . These, along with the standard dissipation rate assumption,

$$\epsilon \sim K^{3/2}/L \quad (9)$$

leads to the classical decay solution of Ref. [2] in which  $U \sim x^{-2/3}$  and  $L \sim x^{1/3}$ . An alternative is the anomalous dissipation rate assumption of Ref. [6],

$$\epsilon \sim U_m DK/L^2, \quad (10)$$

which yields the decay  $U \sim x^{-1}$ , consistent with the experimental data of Ref. [5]. (Note that, in Ref. [6],  $K \sim U_o^2$  and, hence,  $K$  and  $U_o^2$  are interchangeable in Eq. (10).)

Although these six constraints on the six scaling variables yield a unique scaling law, one can instead find a family of scaling solutions if one of these constraints is relaxed. Here, it is proposed (based on the experimental results presented below) that the last term on the right in Eq. (8) can be neglected. This term represents the production of kinetic energy from the radial shear in the mean axial velocity ( $\bar{u}\bar{v} \partial_r U$ ). It could plausibly be negligible compared to the other terms if there is sufficient kinetic energy immediately aft of the generating body such that downstream production does not add significantly to this initial kinetic energy. Then, if one makes the standard dissipation assumption [Eq. (9)], there exists a family of scaling solutions parametrized by the exponent of the wake growth rate with  $x$ , here denoted  $\alpha$ . The scaling exponents corresponding to this solution are listed in Table I, along with the previous classical [1] and anomalous [6] values. The value of  $\alpha = 1/2$  corresponds to the experimental observations of Ref. [5], whereas  $\alpha = 1/3$  yields the classical result. The anomalous scaling of Ref. [6] has the same exponents for the wake size  $L$ , velocity defect  $U_o$ , and Reynolds stress  $R$  as the proposed  $\alpha = 1/2$  solution but yields more rapid decay for the turbulent kinetic-energy  $K$  and dissipation rate  $\epsilon$ . If instead the anomalous dissipation assumption [Eq. (10)] is used in conjunction with the assumption proposed here [that the last term in Eq. (2) is negligible], the exponents for  $L$  and  $U_o$  are still 1/2 and -1, respectively, but the exponents for  $K$  and  $\epsilon$  are undetermined.

For self-consistency, the neglected term in Eq. (2) must decay with  $x$  more rapidly than the other terms. This requires  $\alpha > 1/3$ , which is not surprising since  $\alpha = 1/3$  corresponds to the standard drag wake scaling law in which all terms are in balance [2]. As an upper bound, the requirement that  $K$  decays with  $x$  implies  $\alpha < 1$ .

Table I presents the scaling exponents for each variable in the proposed solution, along with the classical decay law [1,2], the viscous solution of Refs. [12,13], and the anomalous dissipation

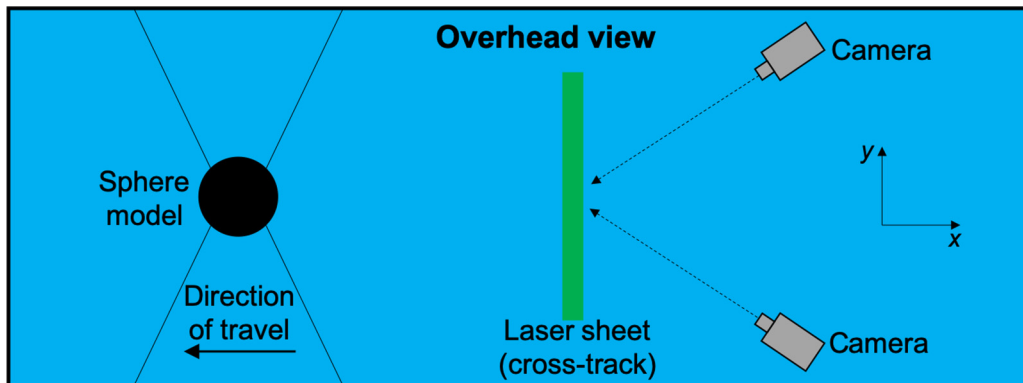


FIG. 1. A schematic of the experimental layout, illustrating the location of the towed sphere, PIV cameras, and orientation of the laser illumination sheet.

assumption of Ref. [6]. For  $\alpha = 1/3$ , the proposed scaling reduces to the classical result as expected. The value of  $\alpha = 1/2$  yields the same mean velocity decay exponent ( $-1$ ) proposed by Refs. [6,12,13]. The Reynolds stress also has the same exponent ( $-3/2$ ) as Ref. [6] but different exponents for the turbulent kinetic-energy ( $-1$  vs  $-2$ ) and the dissipation rate ( $-2$  vs  $-3$ ). An interesting consequence of  $\alpha = 1/2$  is that the Reynolds number based on velocity fluctuations  $Re = K^{1/2}L/\nu$  is independent of  $x$ . (The Reynolds number based on the mean streamwise velocity does decay as observed in Ref. [6]). A constant Reynolds number does not occur in the classical solution for a drag wake ( $\alpha = 1/3$ ) but is a common feature among other similar flows, such as axisymmetric jets and plane wakes [12].

For any value of  $\alpha$  greater than  $1/3$ , the magnitude of the velocity fluctuations  $\sqrt{K}$  decays with exponent  $\alpha - 1$ , which is less rapid than the decay of the ensemble-mean velocity defect (exponent  $-2\alpha$ ). (For  $\alpha = 1/3$ , the two decay with the same exponent  $-2/3$ , maintaining balance between the terms as assumed in the classical solution.) This implies that, as the wake decays, it is increasingly dominated by velocity fluctuations, whereas the mean axial flow becomes relatively insignificant. In the proposed scaling solution, this would apply for the case  $\alpha = 1/2$ , which is consistent with other measurements of axisymmetric wake decay but yields a slower rate of velocity fluctuation decay than the other solutions in Table I with a wake size growth exponent of  $1/2$ .

### III. EXPERIMENTAL APPROACH

Experiments were conducted in a tow tank using a dimpled sphere with a diameter of  $D = 8.5$  cm. The dimples on the sphere serve to trip the boundary layer and increase the level of turbulence in the flow along the sphere body. The dimpled sphere and tank have been used previously to study stratified drag wakes by Ref. [14]. The submerged sphere was towed at a constant speed of  $U_m = 60$  cm/s. The sphere depth was approximately midway between the tank bottom and the free surface where the total fluid depth was 68 cm ( $\sim 8D$ ). Figure 1 presents a schematic overhead view of the experiment. Surface disturbances were not observed during the experiments, indicating that interactions between the wake and the free surface did not occur.

Table II presents the Reynolds number and measurement range of the present paper along with equivalent values and quantities measured from comparable previous experiments [5,6]. With a tow speed of  $U_m = 60$  cm/s, the Reynolds number ( $U_mD/\nu$ ) of the present experiments was 50 000. Other recent experiments on drag wakes indicating nonclassical scaling obtained  $Re = 2000$ – $12\,000$  and  $Re = 10\,000$ , four to five times lower than the Reynolds number achieved here.

SPIV data were acquired immediately following the passage of the sphere until wake structures exited the field of view of the SPIV system. The PIV system consisted of two TSI 630091

TABLE II. Comparison with previous experiments.

Study	Re ( $\frac{U_m D}{\nu}$ )	$x/D$	Quantities measured
Present experiments	50 000	5–200	Mean axial velocity and wake size Velocity fluctuations and length scale
Bonnier and Eiff [5]	2000–12 200	2–30	Mean axial velocity
Nedic <i>et al.</i> [6]	10 000	5–50	Mean axial velocity and wake size

PowerView 4-MP high-speed cameras oriented at an angle of  $30^\circ$  to the along-track axis. This angle is within the optimum range for SPIV systems as determined by Lawson and Wu [15]. The tank was seeded with a combination of 20- and 50- $\mu\text{m}$  particles illuminated by a Litron Nano L 200-15 pulsed Nd:yttrium aluminum garnet laser. This particle size corresponded to a diameter of 2 to 3 pixels, which provides a good balance between pixel locking for smaller particles and a broader displacement peak for larger ones [16–19]. The particles were neutrally buoyant, and the tank was seeded such that each interrogation region contained on average eight to ten particles. The laser sheet thickness was approximately 3 cm, ensuring that the out-of-plane displacement was less than one-quarter of the light sheet thickness. Images of the sphere and the laser sheet in the tank are presented in Fig. 2.

The SPIV processing was performed using an open-source MATLAB code called UVMAT [20]. The UVMAT algorithm first performs PIV processing of the images from a single camera using a dual-pass method where the first pass determines lower-resolution estimates of the velocity field within an interrogation region, whereas the second pass uses the estimates from the first pass to obtain more precise measurements of the velocity field at a higher resolution. The velocity fields from the two cameras are then combined using SPIV to determine all three velocity components within the single plane of data. Table III details the parameters used for the SPIV measurements. Data were acquired with a 20-mm focal length lens on both cameras imaging the  $y$ - $z$  plane, resulting in an overlapped field of view spanning 45 cm in the  $y$  and 35 cm in the  $z$  directions. Two distinct acquisition settings were used to resolve velocities in near ( $x/D < 20$ ) and far ( $x/D > 15$ ) field of the wakes. The first-pass PIV analysis was performed with  $128 \times 128$  pixel interrogation regions with a search-box size of  $147 \times 147$  pixels, a shift of (0,0) pixels, and a 50% overlap of the interrogation regions. The second pass was performed with interrogation regions of  $64 \times 64$  pixels and a 50% overlap, resulting in a velocity vector every 32 pixels in the  $y$  and  $z$  directions. These window sizes ensured

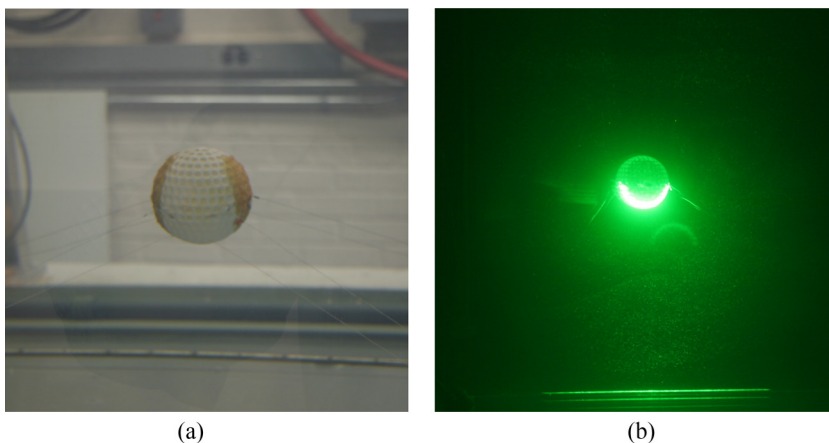


FIG. 2. Images of sphere and laser sheet.

TABLE III. SPIV parameters.

$x/D$ range	Laser pulse rate (Hz)	Image pair time spacing (ms)	Min in plane velocity (cm/s)	Max in plane velocity (cm/s)	Uncertainty (cm/s)	No. of runs
1–20	15	5	1.6	26	0.32	40
15–200	10	10	0.8	13	0.16	42

that particle displacements were limited to  $1/4$  of the interrogation window, corresponding to maximum velocities of 26 and 13 cm/s for the near- and far-field settings, respectively. In practice the minimum observable displacement was less than 1 pixel with displacements of a half pixel corresponding to minimum observable velocities of 1.6 cm/s for the near and 0.8 cm/s for the far-field settings. Typical wake in-plane velocities in these experiments corresponded to particle displacements of 2–5 pixels, depending on the  $x/D$  location. An *a priori* uncertainty quantification of this system yielded maximum uncertainties of less than 0.1 pixels for all displacements. This yields uncertainties of 0.32 cm/s for near- and 0.16 cm/s for far-field in-plane velocities, which are within the range of uncertainties previously reported by others [19]. Additionally, the typical shear across the interrogation window was less than 0.02 pixels.

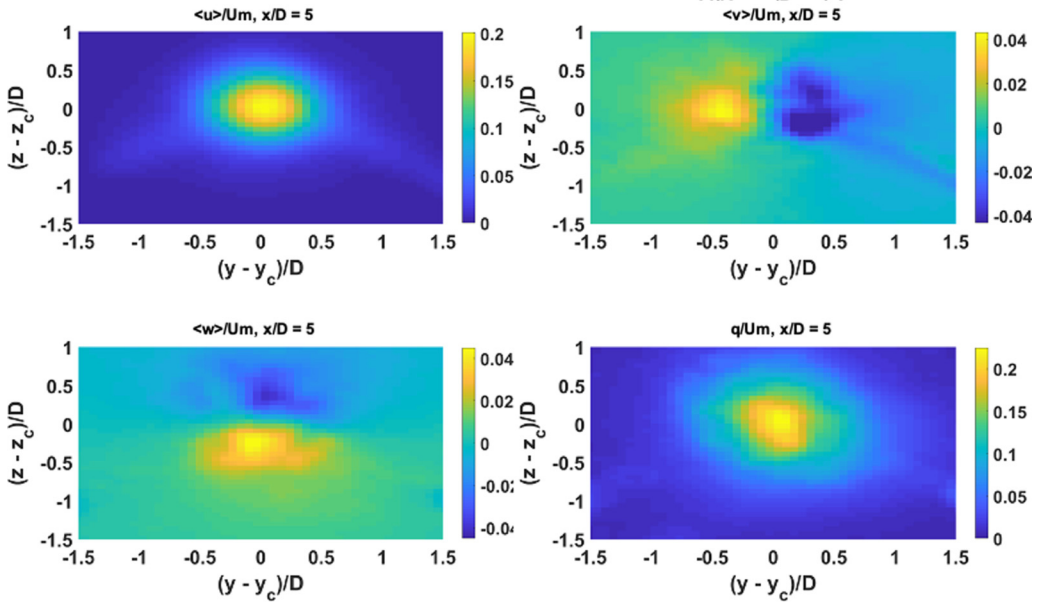
Approximately 40 runs were performed with each field of view so that the results could be combined to produce estimates of the mean and fluctuating velocity fields. To obtain the mean axial velocity, the measured axial velocity fields from each experiment at a given  $x/D$  were averaged. The velocity fluctuation field is simply the standard deviation of the velocity components over the ensemble of experiments at each  $x/D$ . The tow speed varied by less than 1 cm/s between runs so all SPIV velocities were normalized by the nominal tow speed of 60 cm/s. There is also a variation in the depth and horizontal position of the wake center from run to run due to slightly nonzero drift velocities which vary from run to run. This effect was mitigated by averaging the runs together.

#### IV. RESULTS

Figure 3 illustrates the SPIV mean velocity field (averaged over 40 runs) measured at  $x/D = 5$ . The upper left panel shows the mean axial velocity defect, which appears as the yellow region in the center of the panel. This view demonstrates the approximately axisymmetric shape of the axial velocity defect. The two diagonal light-blue lines in the bottom half of the panel are the wakes of the guide wires that tow the sphere, which were excluded from the subsequent quantitative analysis. The upper right and lower left panels present the mean horizontal and vertical velocities, respectively. The lower right panel illustrates the velocity fluctuation over the ensemble of experiments. Figure 4 presents three individual realizations along with the mean flow field (lower right panel). Each individual run contains large deviations (fluctuations) from the ensemble-mean axial velocity (note different color scales for the mean) and do not appear to be axisymmetric. As a result, no individual realization closely resembled the mean flow field. The significant variations among individual realizations is represented by the velocity fluctuation term  $q^2$  in the self-similar theory (Sec. II).

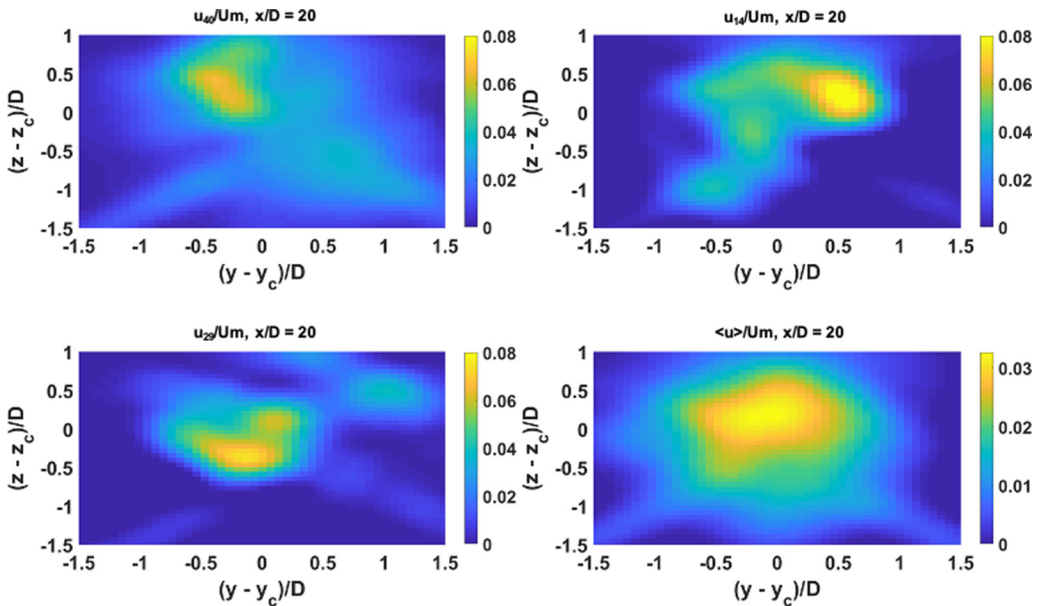
The evolution of the mean axial velocity defect is illustrated in Fig. 5. The wake grows, and its peak velocity decays with distance as expected (note changing color scales). Deviations from axisymmetry tend to increase with down-track distance as more runs are required to obtain a quality estimate of the mean at greater distances. The number of experimental runs limits the distance to which quality results can be obtained.

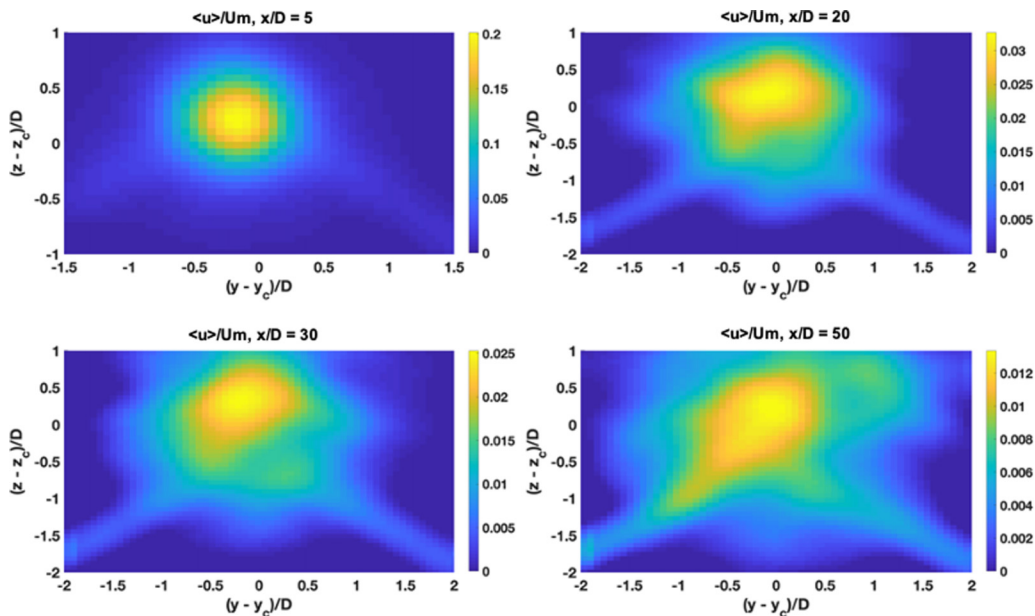
To characterize the wake size and velocity scales as a function of  $x/D$ , the SPIV data are binned into radial bands and averaged over the azimuth to produce radial profiles  $\langle U(r) \rangle$  at each  $x/D$ . To


 FIG. 3. Sphere wake mean velocity components and fluctuations at  $x/D = 5$ .

estimate the length and velocity scale of each profile, the first two moments of the radial profile are computed

$$M_o \equiv \int_0^\infty \langle U(r) \rangle r dr, \quad (11)$$


 FIG. 4. Individual realizations and mean velocity at  $x/D = 20$ .


 FIG. 5. Mean axial velocity defect  $u/U_m$  at four down-track locations.

$$M_2 \equiv \int_0^\infty \langle U(r) \rangle r^3 dr. \quad (12)$$

In practice, the integration range is limited to  $r < 2.5D$  to avoid contamination by noise far from the wake center. ( $M_2$  is somewhat sensitive to the integration limit, but  $M_o$  is not.) Using these, the velocity scale  $U_o$  and size  $L_u$  are computed as

$$L_u^2 \equiv \frac{M_2}{M_o}, \quad (13)$$

$$U_o \equiv \frac{M_o^2}{M_2}. \quad (14)$$

This approach makes no assumption regarding the shape of the velocity profile. Figure 6 presents the wake axial velocity defect profile at several  $x/D$  normalized by the length scale  $L_u(x)$  and velocity scale  $U_o(x)$ . The results demonstrate that the axial velocity defect profile is approximately self-similar when normalized by these scales. Also shown in Fig. 6 is a Gaussian (black line), a shape function frequently used to initialize numerical simulations [21–23]. The data show that the Gaussian is a reasonable approximation to the profile. Approximately Gaussian mean axial velocity defect profile shapes were also reported by Ref. [4] for the drag wake of a slender body, by Ref. [6] for a fractal plate, and by Ref. [13] for a disk.

Variations from the ensemble mean velocity at four  $x/D$  locations are presented in Fig. 7. Here, the fluctuation velocity  $q$  is defined as

$$q^2 \equiv (u - \langle u \rangle)^2 + (v - \langle v \rangle)^2 + (w - \langle w \rangle)^2 \quad (15)$$

representing the root-mean-squared deviation from the ensemble mean. Like the mean velocity defect (Fig. 5), the  $q$  field spreads and decays with down-track distance. However, it lacks the compact core with a single maximum exhibited by the velocity defect. A similar analysis has been performed on the fluctuation velocity  $q$ , which replaces  $U$  in the moment equations [Eqs. (11) and (12)] to yield a second length scale  $L_q^2$  and velocity scale  $Q_o$ . Of course, for self-similar wake

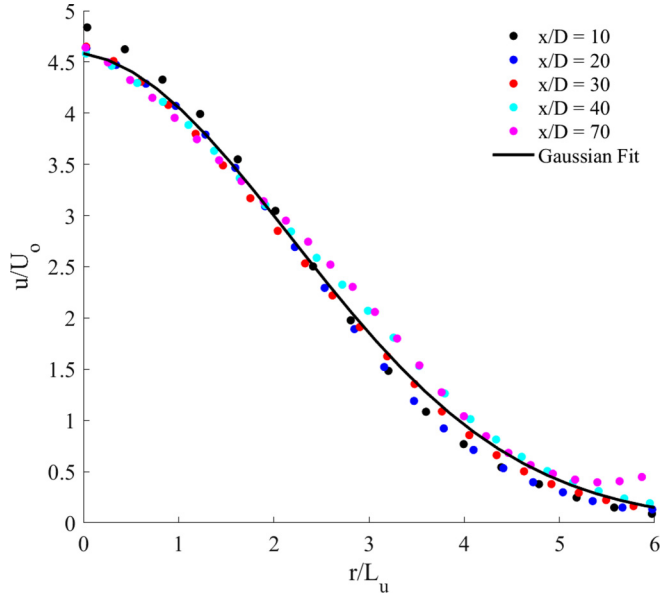


FIG. 6. Self-similar profiles of the mean axial velocity defect  $U/U_0$  as a function of radius  $r/L_u$  at five down-track locations.

decay it is expected that the two length scales are proportional,  $L_q \sim L_u$ . Figure 8 presents the self-similar fluctuation profiles  $q(r/L_q)/Q_0$  for the same  $x/D$  as Fig. 6. Although also approximately self-similar for  $r/L_q < 1.5$ , variations in these profiles are larger than in the defect profiles of Fig. 6

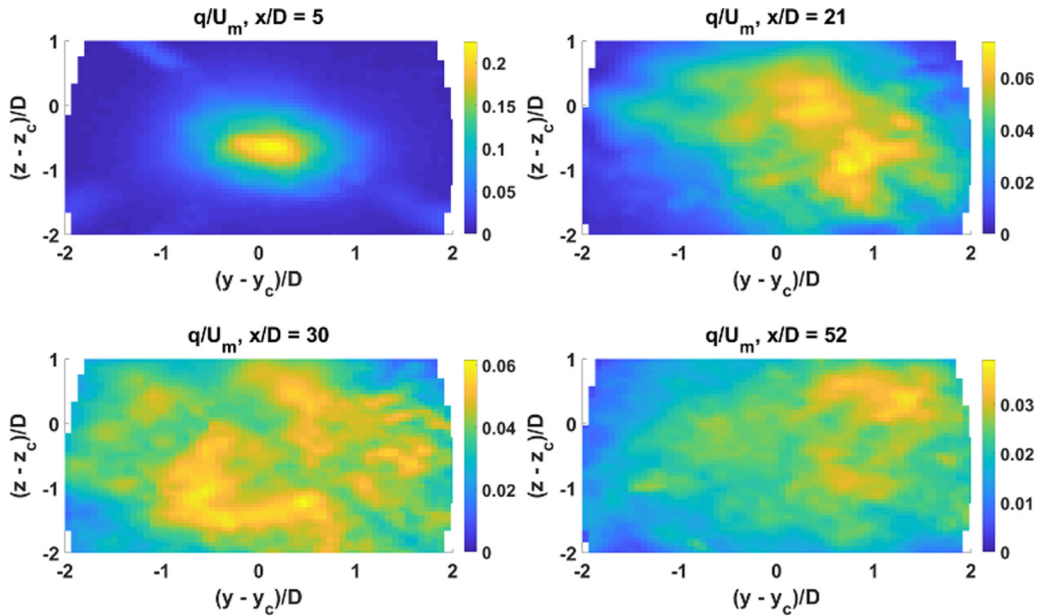


FIG. 7. Velocity fluctuations (defined as the standard deviation from the ensemble mean)  $q/U_m$  at four down-track locations.

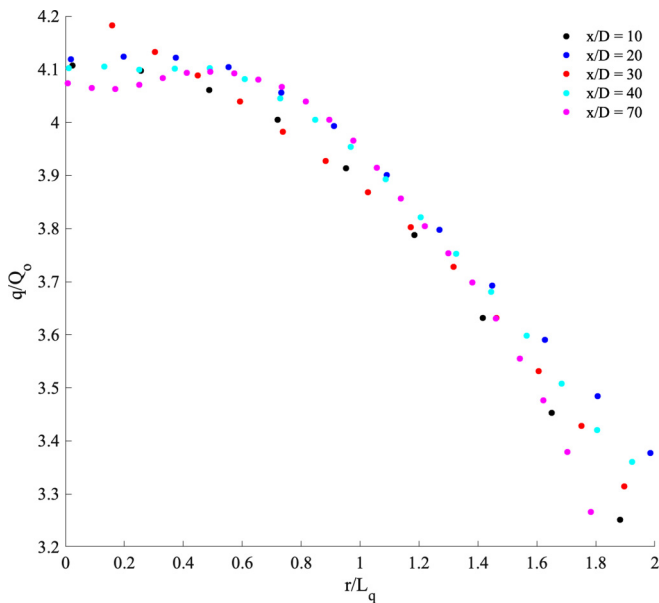


FIG. 8. Self-similar profiles of the velocity fluctuations (defined as the standard deviation from the ensemble mean)  $q/Q_o$ , as a function of radius  $r/L_q$  at five down-track locations.

especially in the wake tails ( $r/L_q > 1$ ). Unlike the mean axial velocity profile, the shape is decidedly non-Gaussian. Non-Gaussian profiles for self-similar fluctuations were also reported for the drag wake of a slender body by [4] and for a disk by Ref. [13].

The decay of the mean axial velocity scale  $U_o$  with  $x/D$  is presented as triangles in Fig. 9. The data were binned using a logarithmic scale with bin width of  $\log_{10}(x/D) = 0.05$ . The error bars in Figs. 9–11 represent one standard deviation of values within each bin. In addition, the decay of the maximum axial velocity at each  $x/D$  bin (analogous to the results of Ref. [5]) and the decay of

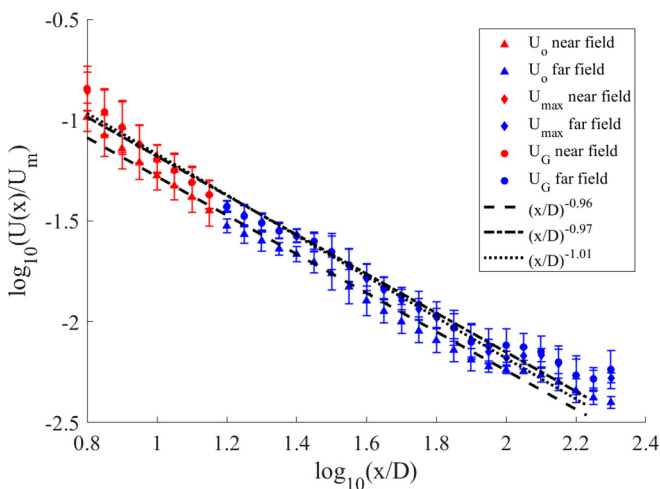


FIG. 9. Axial velocity decay (colored symbols) as a function of  $x/D$  along with best-fit scaling exponents (black lines).

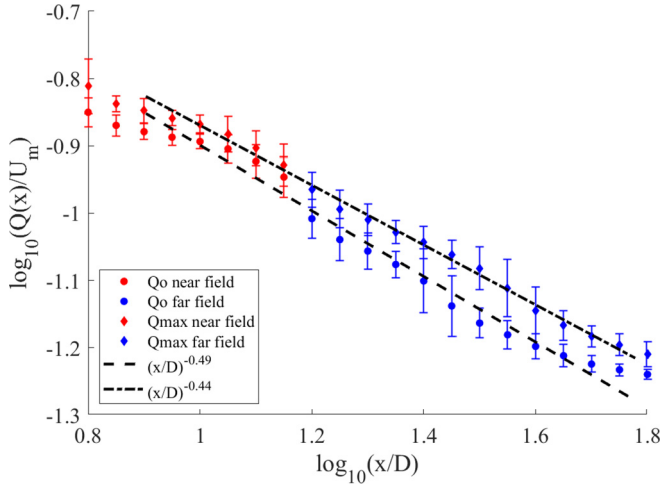


FIG. 10. Velocity fluctuation decay (colored symbols) as a function of  $x/D$  along with best-fit decay exponents (black lines).

the amplitude as determined from a Gaussian fit are included on the plot as diamonds and dotted points, respectively. The three quantities scale together due to self-similarity, whereas the differing approaches confirm the robustness of the scaling. As data were collected using two different SPIV acquisition settings, the results from each are distinguished using red and blue marker colors, respectively. In the vicinity of  $\log_{10}(x/D) \sim 1.2$ , data from both settings are shown. However, the reliability of these data is uncertain as the wake approaches the edge of the smaller field of view (red) whereas some velocity values may exceed the SPIV maximum velocity limit in the larger field of view (blue). The corresponding best-fit scaling exponents over the range  $8 < x/D < 200$  are shown with black lines. The estimated decay exponents are  $-0.96$  for the mean axial veloc-

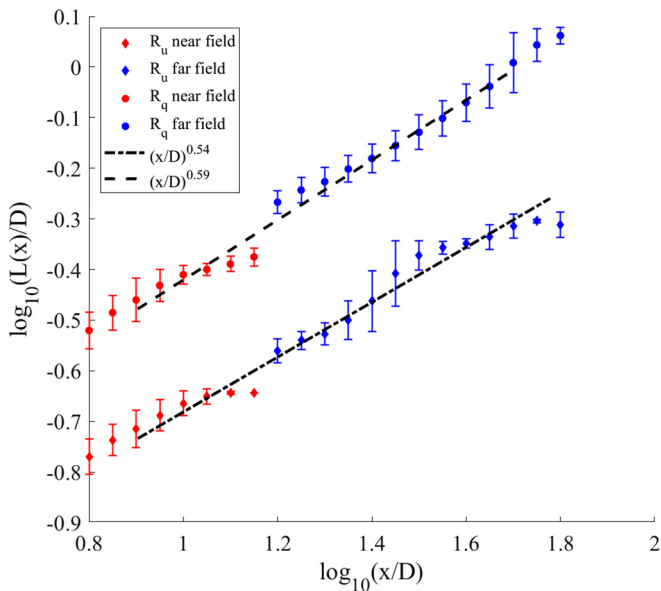


FIG. 11. Wake growth as a function of  $x/D$  along with best-fit growth exponents.

TABLE IV. Exponent comparison: experiment.

Quantity	Size ( $L$ )	Mean velocity ( $U_o$ )	Velocity fluctuations ( $K^{1/2}$ )	Re ( $K^{1/2}L/\nu$ )
<i>Theory</i>				
Classical [1,2]	1/3	-2/3	-2/3	-1/3
Anomalous [6] or viscous [13]	1/2	-1	-1	-1/2
Proposed, $\alpha = 1/2$	1/2	-1	-1/2	0
<i>Experiment</i>				
Present results	$0.54 \pm 0.05$	$-0.96 \pm 0.05$	$-0.49 \pm 0.03$	$0.05 \pm 0.08$
Previous sphere [5]	NA	-0.9 to -1.0	NA	NA
Previous fractal [6]	0.51	-1.01	NA	NA
Previous disk [6]	0.34	-0.68	NA	NA
Previous disk [13]	$\sim 1/3$	$\sim -2/3$	$\sim -2/3$	$\sim -1/3$

ity defect scale  $U_o$ ,  $-0.97$  for the maximum velocity defect  $U_{\max}$ , and  $-1.01$  for the Gaussian fit  $U_G$ .

The decay of the fluctuation velocity scale  $Q_o$ , which reflects the deviations from the ensemble mean and is interpreted as  $\sqrt{K}$  in the previous scaling analysis, is presented in Fig. 10. The scale  $Q_o$  is also representative of the typical velocities in an individual wake realization. In addition, the maximum fluctuation velocity scale at each  $x/D$  bin is included as  $Q_{\max}$ , which follows a similar decay law. The fluctuation velocity  $Q_o$  decays more slowly with  $x/D$  than  $U_o$  with a decay exponent of  $-0.49$ . Again, the two differing approaches are used to confirm the scaling, but the Gaussian fit is not used here as the shape profile is not Gaussian (see Fig. 8).

Figure 11 presents the length scales  $L_u$  and  $L_q$  along with best-fit scaling exponents. The velocity defect scale  $L_u$  increases with  $x/D$  with an exponent of  $0.54$ , whereas  $L_q$  has a similar value of  $0.59$ . Momentum conservation requires that the exponent for  $L_u$  be half the value of the exponent for  $U_o$ , which approximately holds. Self-similarity requires that these two exponents are equal as there should be only one length scale (up to a constant of proportionality), and the data appear relatively consistent with this assumption. The fluctuation length scale  $L_q$  is typically about twice as large as  $L_u$ , but the growth exponents are comparable.

The range for fits was chosen to include as much of the data as possible, however, some data were unreliable and had to be excluded.  $U_o$  and  $U_{\max}$  had the largest range, extending from  $8 \leq x/D \leq 200$  whereas the fits for  $Q_o$  and  $Q_{\max}$  stopped at  $x/D \approx 60$ . The smaller range for  $Q$  was due to worsening statistical convergence as downstream distance increased. The range of valid data for  $L_u$  and  $L_q$  was also  $8 \leq x/D \leq 60$ . This reduced range is due to a combination of the increased sensitivity of (13) to the integration limit and the limited field of view for the SPIV system. Consequently, the confidence in the scaling exponents for  $Q$  and especially  $L$  is less than for  $U$ .

Table IV summarizes the wake scaling exponents found in the present paper, compared to previous studies and theoretical self-similar scaling laws. The axial velocity decay scaling exponent is consistent with previous experiments for spheres [5] and fractal disks [6] at somewhat smaller Reynolds numbers. The wake size exponent is also consistent with Ref. [6] but was not measured by Ref. [5]. However, the axial velocity decay and wake size scaling exponents differ from the classical scaling experiments found in the disk experiments of Refs. [6,13], included as the last two lines in Table IV. (Best-fit exponents were not reported by Ref. [13], but the results were shown to be consistent with classical scaling.) The estimated measurement of the decay exponent for velocity fluctuations is novel for a sphere. For comparison, theoretical values for the same exponents are shown for three different assumptions for self-similar decay. The results found here, such as the previous experiments, are inconsistent with the classical scaling of Refs. [1,2]. Although the mean axial velocity results are consistent with the anomalous dissipation hypothesis of Ref. [6], the viscous scaling of Ref. [13], and the conjecture proposed here with  $\alpha \simeq 1/2$ , the decay exponent for

velocity fluctuations is closer to the present conjecture than the alternatives. Indeed, this observation regarding decay of turbulent fluctuations motivated the proposed conjecture. Note also that the Reynolds number based on the velocity fluctuations is approximately preserved with downstream distance in the present experiments.

## V. DISCUSSION

This is an experimental study demonstrating sphere drag wake decay exponents over more than a decade of scaling ( $8 \leq x/D \leq 200$ ) which differ from the long-standing and generally accepted classical self-similar scaling exponents [1,2]. The results are consistent with other axisymmetric drag wake experimental results [5,6] obtained over much smaller ranges of downstream distances with a mean velocity defect decay exponent of  $\sim -1$  and wake size growth exponent of  $\sim 1/2$ . The present results demonstrate that this nonclassical scaling exponent is not merely a near-wake or transitory effect, confined to the the first few tens of diameters downstream.

New results for velocity fluctuations, which were found to decay more slowly than the ensemble-mean axial velocity defect, provide an additional point of comparison for competing theoretical explanations of axisymmetric drag wake decay. The observed decay exponent for velocity fluctuations appears inconsistent with the balance between production from mean shear and fluctuation magnitude assumed in most other solutions [1,2,6,13]. The ratio of velocity fluctuations to the mean axial velocity increases with downstream distance, suggesting that one of the terms in the mean energy equation is not in balance with the others. Relaxing the common assumption that all terms in the mean flow equations are in balance permits self-similar solutions with nonclassical decay exponents whereas preserving the standard Kolmogorov dissipation scaling. However, the experimental data for the mean velocity decay are not inconsistent with the solution of Ref. [6] in that this kinetic-energy balance is not essential to obtaining the  $-1$  exponent for mean axial velocity decay if anomalous dissipation is assumed. The approach of Ref. [6] does not appear to yield a complete self-similar solution without relying on this assumption, as the kinetic-energy decay exponent cannot be determined without it, and the exponent obtained using this assumption is not consistent with the experimental data.

Previous experimental measurements of the wakes of disks have yielded classical scaling [6,13]. In addition to using a different shape body (disk vs sphere in the present experiments), these experiments were conducted at somewhat lower Reynolds numbers and were performed in wind tunnels, which typically have some inflow turbulence, unlike the quiescent water in the tow tank experiments reported here. Results for the decay of velocity fluctuations in the wake of a disk are also reported in Ref. [13] and are consistent with classical scaling (unlike the present results for a sphere). Contrasting the results in Table IV for decay and spread of the mean axial flow velocities suggests the shape plays a role in the decay and spreading of the wake. The results of Ref. [6] in which the same wind tunnel facility yielded classical decay for a disk and decay consistent with the present results for a fractal shape supports the conjecture that different body shapes may yield different wake decay exponents.

The observed nonclassical decay of the velocity fluctuations yields a Reynolds number  $Re = K^{1/2}L/\nu$  which is approximately independent of  $x$ . A constant Reynolds number does not occur in other proposed self-similar solutions for a drag wake but is a common feature among other similar flows, such as axisymmetric jets and plane wakes [12]. Whether the observed scaling persists indefinitely, or transitions to the classical law as suggested by Ref. [8] are not known, but no evidence of a transition was observed prior to  $x/D \sim 200$ .

Another key observation from the data is that the drag wake is increasingly dominated by fluctuations (rather than the mean) as it decays. A consequence of this is that no individual wake realization bears much resemblance to the mean. This suggests that mean-field characterizations of the axisymmetric drag wake as used here may not be the most informative way to describe wake dynamics. Instead, some measure of a typical wake's characteristics may be more meaningful. It is also worth noting that Reynolds-averaged Navier-Stokes simulations, commonly used in

engineering work, essentially adopt the mean-field approach, solving for the mean axial velocity. As such, the output of such simulations might also not be very representative of a typical drag wake.

#### ACKNOWLEDGMENT

This work was funded by the JHU/APL IRAD Program.

- 
- [1] L. M. Swain, On the turbulent wake behind a body of revolution, *Proc. R. Soc. London A* **125**, 647 (1929).
  - [2] H. Tennekes and J. L. Lumley, *A First Course in Turbulence* (MIT Press, Cambridge, MA, 1972).
  - [3] P. M. Bevilaqua and P. S. Lykoudis, Turbulence preservation in self-preserving wakes, *J. Fluid Mech.* **89**, 589 (1978).
  - [4] Y.-H. Pao and J.-T. Lin, Velocity and density measurements in the turbulent wake of a towed slender body in stratified and nonstratified fluids, *Flow Res. Rep.* **12**, 1 (1973).
  - [5] M. Bonnier, and O. Eiff, Experimental investigation of the collapse of a turbulent wake in a stably stratified fluid, *Phys. Fluids* **14**, 791 (2002).
  - [6] J. Nedić, J. C. Vassilicos, and B. Ganapathisubramani, Axisymmetric Turbulent Wakes with New Nonequilibrium Similarity Scalings, *Phys. Rev. Lett.* **111**, 144503 (2013).
  - [7] A. Pal, S. Sarkar, A. Posa, and E. Balaras, Direct numerical simulation of stratified flow past a sphere at a subcritical Reynolds number of 3700 and moderate Froude number, *J. Fluid Mech.* **826**, 5 (2017).
  - [8] K. Chongsiripinyo and S. Sarkar, Decay of turbulent wakes behind a disk in homogeneous and stratified fluids, *J. Fluid Mech.* **885**, A31 (2020).
  - [9] P. C. Valente and J. C. Vassilicos, Universal Dissipation Scaling for Nonequilibrium Turbulence, *Phys. Rev. Lett.* **108**, 214503 (2012).
  - [10] T. Dairay, M. Obligado, and J. C. Vassilicos, Non-equilibrium scaling laws in axisymmetric turbulent wakes, *J. Fluid Mech.* **781**, 166 (2015).
  - [11] W. J. T. Bos and R. Rubinstein, Dissipation in unsteady turbulence, *Phys. Rev. Fluids* **2**, 022601(R) (2017).
  - [12] W. K. George, The self-preservation of turbulent flows and its relation to initial conditions and coherent structures, in *Advances in Turbulence*, edited by W. K. George and R. Arndt (Hemisphere, New York, 1989), pp. 39–73.
  - [13] P. B. V. Johansson, W. K. George, and M. J. Gourlay, Equilibrium similarity, effects of initial conditions and local Reynolds number on the axisymmetric wake, *Phys. Fluids* **15**, 603 (2003).
  - [14] A. Brandt and J. R. Rottier, The internal wavefield generated by a towed sphere at low Froude number, *J. Fluid Mech.* **769**, 103 (2015).
  - [15] N. J. Lawson and J. Wu, Three-dimensional particle image velocimetry: experimental error analysis of a digital angular stereoscopic system, *Meas. Sci. Technol.* **8**, 1455 (1997).
  - [16] J. Westerweel, Digital Particle Image velocimetry - Theory and application, Ph.D. thesis, Delft University, 1993, <http://resolver.tudelft.nl/uuid:85455914-6629-4421-8c77-27cc44e771ed>.
  - [17] J. Westerweel, Fundamentals of digital particle image velocimetry, *Meas. Sci. Technol.* **8**, 1379 (1997).
  - [18] R. J. Adrian and J. Westerweel, *Particle Image Velocimetry* (Cambridge University Press, New York, 2011).
  - [19] A. Sciacchitano, Uncertainty quantification in particle image velocimetry, *Meas. Sci. Technol.* **30**, 092001 (2019).
  - [20] UVMAT Particle Image velocimetry program, <http://servforge.legi.grenoble-inp.fr/projects/soft-uvmat>.
  - [21] M. B. de Stadler, S. Sarkar, and K. A. Brucker, Effect of Prandtl number on a stratified turbulent wake, *Phys. Fluids* **22**, 095102 (2010).
  - [22] P. J. Diamessis, G. R. Spedding, and J. A. Domaradzki, Similarity scaling and vorticity structure in high-Reynolds-number stably stratified turbulent wakes, *J. Fluid Mech.* **671**, 52 (2011).
  - [23] K. L. Rowe, P. J. Diamessis, and Q. Zhou, Internal gravity wave radiation from a stratified turbulent wake, *J. Fluid Mech.* **888**, A25 (2020).